A coupled hydro-structural design optimization for hydrokinetic turbines

Nitin Kolekar and Arindam Banerjee

Additional information on J. Renewable Sustainable Energy

A coupled hydro-structural design optimization for hydrokinetic turbines

Nitin Kolekar and Arindam Banerjee[a]
*Department of Mechanical Engineering and Mechanics, Lehigh University,
Bethlehem, Pennsylvania 18015, USA*

An optimization methodology for a stall regulated, fixed pitch, horizontal axis hydrokinetic turbine is presented using a combination of a coupled hydro-structural analysis and Genetic Algorithm (GA) based optimization method. Design and analysis is presented for two different designs: a constant chord, zero twist blade, and a variable chord, twisted blade. A hybrid approach is presented combining Blade Element Momentum (BEM), GA, Computational Fluid Dynamics (CFD), and Finite Element Analysis (FEA) techniques. The preliminary analysis is performed using BEM method to find the hydrodynamic performance and flap-wise bending stresses in turbine blades. The BEM analysis used for the current study incorporates effect of wake rotation, hub loss and tip loss factors, and effect of Reynolds number on hydrodynamic data. A multi-objective optimization is then performed to maximize performance and structural strength of turbine. The results of optimization for a constant chord, zero twist blade design are validated with detailed three dimensional CFD and finite element analysis. The fluid domain is coupled with the structural domain through one way coupling and fluid-structure interaction analysis is carried out to find the effect of blade geometry and operating conditions on the stresses developed in the blades. The hydrodynamic performance of a constant chord turbine was found to be limited by the high stresses developed in turbine blades. Hence, in an effort to reduce the stresses in turbine blades, a variable chord, twisted blade design was developed; and a multi-objective optimization is presented for the variable chord twisted blade turbine for hydro-structural performance improvement. The final-optimized variable chord, twisted blade design was found to improve the power coefficient by 17% and resulted in lower overall stresses. © 2013 AIP Publishing LLC.
[http://dx.doi.org/10.1063/1.4826882]

I. INTRODUCTION

Hydrokinetic turbines (HKTs) are a class of low head energy conversion devices which convert kinetic energy of flowing water in rivers, tides, and ocean waves into mechanical work that is then converted to electrical power by suitable power-take off devices.[1,2] The operating principle of HKTs is similar to wind turbines which are lift/drag devices as compared to conventional hydro-turbines which operate under large heads (>10 m).[3,4] Traditionally, hydropower has accounted for the bulk of the renewable energy production in the United States. The total electricity use in the U.S. in 2011 was 3856 TWh/yr with $\sim$9% of that output coming from renewables; traditional hydroelectric or micro-hydro facilities contributing $\sim$35% of the total renewable energy production.[5] However, growth of conventional hydropower plants is constrained by the number of available natural sites, large capital (initial) investment, extensive pay-back time, and environmental concerns.[6,7] In lieu of this, marine and hydrokinetic systems

[a]Author to whom correspondence should be addressed. Electronic mail: arb612@lehigh.edu. Tel.: (610) 758-4099, Fax: (610) 758-6224. Present address: Packard Laboratory, Lehigh University, Bethlehem, Pennsylvania 18015-3085, USA.

offer many advantages as these are portable systems with small initial set-up costs that do not require large infrastructure and can be quickly deployed.[1,2,6,8,9] A study conducted by Electric Power Research Institute (EPRI) for U.S. rivers estimated the total technically recoverable hydrokinetic power at 120 TWh/yr ($\sim$3% of the total electricity use) with the Lower Mississippi region contributing nearly 48% and Alaska region constituting $\sim$17% of the total resource estimate.[10] Another study conducted by EPRI evaluated many, but not all tidal energy sites in U.S. and estimated 250 TWh/yr of tidal energy ($\sim$6% of the total electricity use) with 94% of the available energy in Alaska and the remaining 6% in continental United states (mostly in Washington and Maine).[11]

HKTs are lift/drag devices similar to wind turbines, and their performance is governed by several non-dimensional quantities: (i) the tip-speed ratio ($TSR : \lambda = \frac{R\Omega}{U}$), which is defined as ratio of blade tip speed to fluid speed (U) (where R is turbine radius) and Ω is the rpm; (ii) solidity ($\sigma = \frac{Bc}{2\pi R}$) that is defined as the ratio of the product of the blade chord length (c) and the number of blades (B) to the turbine circumference; and (iii) the chord Reynolds number ($Re = \rho Uc/\mu$), where ρ and μ are the density and viscosity of the fluid medium. Over the last decade, the flow-dynamics of wind turbines and HKTs have been investigated using computational fluid dynamics (CFD)[4,12,13] and laboratory scale experiments.[14–18] Blade-element-momentum (BEM) analysis which forms the backbone of wind turbine rotor design can also be used for HKTs design.[19] Apart from BEM, low-order CFD tools like vortex and panel methods can be used for hydrodynamic analysis of these devices.[20–23] In addition, computationally expensive higher-order techniques that involve solving Reynolds-averaged-Navier-Stokes equations (RANS) and large eddy simulations (LES) with turbulence models have been successfully used for hydrodynamic analysis of HKTs.[4,13,17,24–28] Consul et al.[4] performed a two dimensional CFD analysis to understand the influence of number of blades on performance of cross flow turbines and found improved performance with a higher number of blades. Hwang et al.[29] investigated the effect of variation of TSR, chord length, number of blades, and the shape of hydrofoil on performance of a variable pitch vertical axis water turbine using both experiments and numerical calculations. Duquette and co-workers[12,13] performed experiments and 2-D numerical analysis to study the effect of number of blades and solidity on the performance of a horizontal axis wind turbine. Their analysis concluded that the range of TSR for maximum C_p depends strongly on solidity and weakly on the number of blades. This indicates the chord length plays an important role in defining the optimum TSR range that leads to maximizing the turbine performance. Mukherji et al.[24] performed three-dimensional steady-state CFD to understand effect of TSR, solidity, blade pitch, and number of blades on performance of HKTs and reported a strong influence of TSR on performance coefficient for various turbine geometries. Further, increase in turbine solidity and blade numbers were reported to maximize the C_p that was observed at lower TSR. Batten et al.[28] used a coupled actuator disc-RANS based model to predict the performance and loads on a tidal turbine and obtained up to 94% agreement between numerical and experimental velocity variation measured along the centerline of the wake. LES performed by Churchfield et al.[27] reported the presence of lateral asymmetric wake behind turbine which was a result of interaction between inlet shear flow and wake rotation. Myers and Bahaj[14–16] experimentally investigated the flow field and wake recovery behind marine current turbines using mesh disk simulators and found that recovery depends on proximity to water surface, sea bed roughness (which governs vertical velocity profile and turbulent kinetic energy of flow) and to a lesser extent on rotor thrust. Neary et al.[18] performed experiments on an axial flow hydrokinetic turbine in a large open channel to measure velocity and turbulence quantities behind the turbine using an acoustic Doppler velocimeter and a pulse coherent acoustic Doppler profiler techniques. A flow recovery of 80% was reported at ten diameters downstream the rotor plane. Stallard[30] performed experiments with an array of turbines to investigate turbine interactions and the influence of bounding surfaces (free surface and bed) on wake structure behind tidal turbines.

A large majority of the available literature on HKTs focuses on the hydrodynamics and blade optimization for improving the hydrodynamic performance and does not consider fluid structure interaction (FSI) analysis. The interaction of fluid flow with the turbine structure is an

important aspect of design for HKTs due to a denser working medium. This coupled FSI problem can be solved traditionally by two different approaches: (a) a monolithic approach in which governing equations for the structure and flow field are solved simultaneously using a single solver and (b) a partitioned approach in which two distinct solvers are used to independently solve two sets of governing equations described in Sec. II.[31–33] Young[34] performed FSI analysis on carbon fiber composite blades for a marine propeller by combining boundary element and finite element (FEA) methods and validated his computational results with experimental studies. Young *et al.*[22] performed a coupled boundary element-FE hydro-elastic transient analysis of tidal/marine current turbines and compared results with tow-tank experiments. He *et al.*[35] performed a hydro-elastic optimization of a composite marine propeller in a non-uniform wake using CFD-FEA coupled analysis. Compared to the initial blade design, the final design with optimized ply angle and stacking sequence was reported to have 70.6% reduction in vibratory loads. Selig and Coverstone-Carroll[36] used a genetic algorithm (GA) for optimizing annual energy production (AEP) and cost of energy of low-lift airfoils for stall regulated wind turbines and found that AEP is more sensitive to rotor radius than the peak power. Belesis[37] presented GA for constrained optimization of stall regulated wind turbine and found it to be superior to classical optimization methods. GA implementation was reported to have 10% gain in the energy production for different sized stall regulated wind turbines. Fuglsang and Madsen[38] performed multi-disciplinary optimization on stall regulated horizontal axis wind turbine considering fatigue, maximum load, and AEP. They used sequential linear programming and method of feasible directions for optimizations. Operating parameters like TSR, blade pitch as well as blade geometry were found to have a significant effect on performance as well as structural strength of the turbines.

To the knowledge of the authors, the current work presents the first coupled fluid structure interaction analysis for a hydrokinetic turbine for maximizing its hydrodynamic performance and minimizing hydrodynamic stresses on a stall regulated, fixed pitch, horizontal axis hydrokinetic turbine through a coupled hydro-structural analysis and GA based optimization technique. The analysis is performed for two different blades: a constant chord, zero twist design and a variable chord, twisted design. Figure 1 shows a flow chart for the design approach that has been adopted in this paper. As a starting point, a hydrodynamic analysis was carried out using BEM theory to study the effect of various operating parameters on the forces and torque developed on turbine blades for a constant chord turbine. During the preliminary design process when a detailed flow field solution is not available, stresses in the turbine blade are computed based on forces obtained from BEM. The turbine blade was modeled as a cantilever beam fixed at the hub; stresses were calculated based on blade section area. The hydro-structural optimization was carried out for a constant chord blade turbine using GA in MATLAB optimization toolbox. A Pareto optimal solution set obtained from GA was used as an input to the coupled FSI analysis. To check the fidelity of BEM and the optimized design, the results of lower order BEM model for a constant chord blade design are compared with a detailed three-dimensional coupled CFD-FEA analysis. The CFD domain is coupled with the structural domain using an arbitrary Lagrangian-Eulerian scheme and FEA is performed to find deflection and stresses in the turbine components. The results of structural analysis are then used to modify the turbine geometry and design space for hydro-structural optimization, imposing limits on operating parameters and size. Further to improve the structural strength of the turbine blade, a chord and twist distribution is added to the turbine blade. A multi-objective (hydro-structural) optimization was performed for this variable chord twisted blade geometry to maximize hydrodynamic performance and minimize structural stresses in turbine blade. Higher flow velocities (>3.5 m/s) and proximity to water surface were found to cause cavitation on turbine blades.[22] The current analysis assumes a flow speed of 2 m/s and that the turbine was submerged sufficiently in water and away from free water surface to provide a cavitation free environment for turbine operation. The HKT design presented in this paper has three blades made from a hydrofoil shape and connected at the turbine hub similar to a typical horizontal axis wind turbine. HKTs are lift-drag devices and operate on a similar working principle as the wind turbines; however, a denser working medium (water which is almost 800 times denser than the air) poses additional
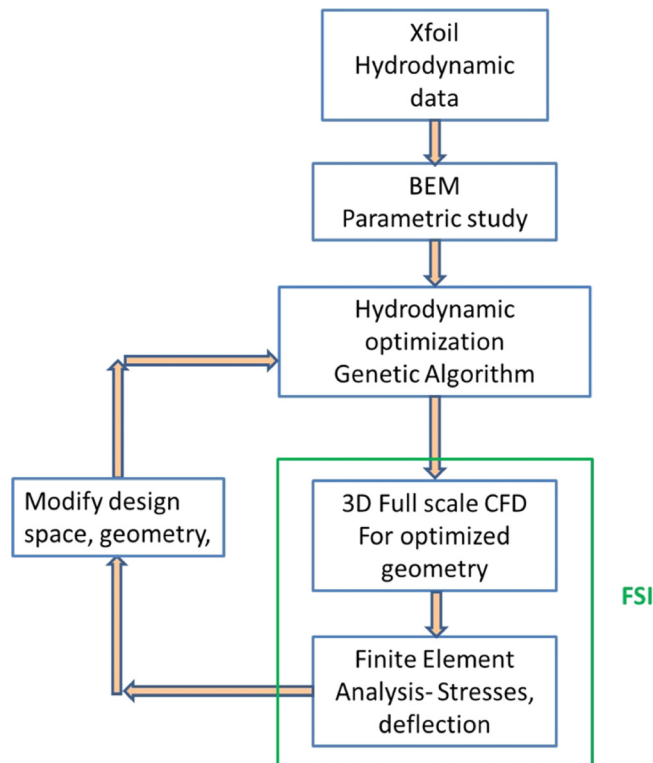
FIG. 1. Hydro-structural optimization and design method for HKTs.

challenges as the flow Reynolds number and the associated hydrodynamics for these turbines are different than that for conventional wind turbines. A CFD analysis and validation is performed to address the effect of change of working fluid (viscosity and density) that affect flow parameters like flow separation and stall delay that in turn affects the performance. A denser working fluid results in higher power density per unit swept area that induces a higher stress state in the turbine blades. The investigation of this stress field is one of the primary objectives of the current fluid-structure interaction analysis.

II. THEORY AND MATHEMATICAL MODEL

A. BEM theory

BEM theory, originally attributed to Betz[39–41] and Glauert,[19] is a combination of blade element theory and momentum theory. According to the blade element theory, forces on a turbine blade can be obtained by dividing the blade into a number of hydrodynamically independent elements.[42] Hydrodynamic forces on these elements are calculated based on local flow conditions using two dimensional lift-drag data. The forces on each element are then summed together to find total force on the turbine blade. The other part of BEM, known as momentum theory, assumes that the work done by the fluid on the turbine blade creates pressure (or momentum) loss across the rotor plane. Induced velocities in axial and tangential direction can be calculated from this momentum loss, which in turn affects the forces on turbine blade. BEM combines blade element and momentum theories and solves coupled equations in an iterative manner to determine fluid forces (thrust and torque) and induced velocities near the rotor.[42] Aerodynamic data: lift coefficients (C_L) and drag coefficients (C_d) for the SG6043 hydrofoil that were adopted for our HKT blades are obtained from Xfoil.[43] These coefficients were then used to calculate forces on blade element in directions normal and tangential to the rotor plane. Xfoil calculates lift and drag forces on a given hydrofoil by combining a linear-vorticity stream function panel method[44] and a viscous solution method. A surface transpiration model is used

to couple a viscous solution (for boundary layer and wake) with an incompressible potential flow solution (for the flow domain away from the turbine surface). Hydrodynamic data obtained from Xfoil is corrected according to Refs. 12 and 13 as

$$C_d = C_{d,\text{Re}_{\text{Ref}}} \left(\frac{\text{Re}_{\text{Ref}}}{\text{Re}} \right)^{0.2}, \tag{1}$$

which suggests that the drag coefficient scales inversely with Reynolds number. The drag coefficient, C_d, in Eq. (1) is the actual drag coefficient (based on Re), $C_{d,\text{Re}_{\text{Ref}}}$ is the drag coefficient based on Re_{Ref} which is the reference Reynolds number (2.4×10^5) used during BEM analysis. The lift coefficient is assumed to be unchanged with Reynolds number.[13] This correction is valid for a Reynolds number range $(10^5 < Re < 10^7)$ which covers the current operating range $(1 \times 10^5 < Re < 5 \times 10^5)$. The Reynolds number reported in the present work is based on the free stream flow speed (U) and the blade mean chord-length (c_m). The Re based on mean chord lengths of 0.05 m and 0.25 m are $\sim 1 \times 10^5$ and $\sim 5 \times 10^5$, respectively.

For our analysis, the original BEM theory of Betz[39,40] and Glauert[19] was modified to take into account the effect of hub, tip, and Reynolds number dependence for hydrodynamic data correction. Prandtl's tip loss correction factor (F_{Tip}) was incorporated in the algorithm to account for losses due to fluid flow from pressure side to suction side at blade tip while the hub loss (F_{Hub}) correction factor was also incorporated to account for losses caused by swirling flow due to presence of hub as

$$F_{Tip} = \frac{2}{\pi} \cos^{-1} \left(\exp \left(\frac{B(r-R)}{2r\sin(\phi)} \right) \right); \quad F_{Hub} = \frac{2}{\pi} \cos^{-1} \left(\exp \left(\frac{B(r_{hub}-r)}{2r_{hub}\sin(\phi)} \right) \right), \tag{2}$$

where r is the radius at the blade element [m], r_{hub} is the hub radius [m], and ϕ is the angle of relative flow [radians].

The effects of correction factors for tip and hub losses are combined into single factor F $(=F_{tip} \times F_{hub})$ that is used to determine net thrust (T) and torque (Q) from turbine

$$T = \int_{r_{hub}}^{R} F\rho U^2 4a(1-a)\pi r dr; \quad Q = \int_{r_{hub}}^{R} 4Fa'(1-a)\rho U\pi r^3 \Omega dr, \tag{3}$$

where ρ is the water density [kg/m^3]. The axial induction factor (a) is defined as fractional decrease in water velocity between the free stream and the rotor plane. The angular induction factor (a') is defined as one half the ratio of the angular velocity of the wake to the angular velocity of the rotor $\left(a' = \frac{\omega}{2\Omega} \right)$.

Preliminary structural analysis is based on an assumption that the turbine blade can be modeled as a cantilever beam supported at blade root and flap-wise bending moment can be found from thrust forces acting on blade. Flap-wise bending stresses in the turbine blade depend on the thrust force and are determined according to Eq. (5)

$$M_\beta = \frac{1}{B} \int_0^R r dT; \quad \text{where,} \quad dT = \left(\frac{1}{2} \rho \pi C_T U^2 2r dr \right).$$

On integration

$$M_\beta = \frac{2}{3} \frac{T}{B} R, \tag{4}$$

$$\sigma_{\beta,\max} = \frac{M_\beta c}{I_b}, \tag{5}$$

where I_b is the area moment of inertia of blade cross-section (airfoil shape) [m^4], M_β is the flap-wise bending moment [N/m], $\sigma_{\beta,\max}$ the maximum flap-wise stress [N/m^2], and, C_T is the thrust coefficient that was assumed as 8/9 for an ideal rotor.[42]

B. FSI-governing equations

FSI problem involves the fluid domain and structural domain interacting with each other at the fluid-structure interface. The load transfer at the interface is done using Arbitrary Lagrangian-Eulerian (ALE) formulation.[31–33,45] This section briefly summarizes the governing equations for the fluid and structural solvers.[45,46] The subscript (*f*) denotes quantities related to the fluid domain and the subscript (*s*) denotes structural domain quantities. The fluid-structure interface is the common boundary between the two domains where data transfer takes place.

1. Computational fluid dynamics:

A three-dimensional CFD analysis was performed in ANSYS CFX using a multiple reference frames technique.[47,48] A rotating reference frame was incorporated to take into account the effect of turbine rotation by transforming an unsteady flow in an inertial (stationary) frame to a steady flow in a non-inertial (moving) frame using equations below[32,33,45,49]

$$\nabla \cdot \vec{U}_r = 0, \tag{6}$$

$$\left[\frac{\partial}{\partial t}(\rho\vec{U}) + \nabla \cdot (\rho\vec{U}_r\vec{U}) + \rho(\vec{\Omega} \times \vec{U}_r + \vec{\Omega} \times \vec{\Omega} \times \vec{r}) \right] = -\nabla p + \nabla \cdot \tau_f, \tag{7}$$

where $\vec{U}_r$ $(= \vec{U} - \vec{\Omega} \times \vec{r})$ is the relative velocity viewed from rotating reference frame, $\vec{\Omega}$ is the rotational speed of the turbine, $\rho(\vec{\Omega} \times \vec{U}_r)$ is the Coriolis force, $\rho(\vec{\Omega} \times \vec{\Omega} \times r)$ is the centrifugal force, τ_f is viscous stress tensor, ∇p is the pressure gradient across the turbine. The viscous stress tensor (τ_f) is defined as

$$\tau_f = \mu_{eff} \left[(\nabla\vec{U} + \nabla\vec{U}^T) - \frac{2}{3}\nabla \cdot \vec{U}I \right], \tag{8}$$

where U is the absolute fluid velocity and I is the identity tensor. The effective viscosity (μ_{eff}) is the sum of the molecular viscosity (μ) and turbulent viscosity (μ_t); μ_t being calculated from a representative turbulence model. A k-ω SST (Shear Stress Transport) turbulence model was chosen due to its accuracy for adverse pressure gradient flows as the current case.[50–52] The computational domain consists of an inner rotating sub-domain of size $1.1R \times 0.65$ and an outer stationary sub-domain of size $6R \times 22$. Fig. 2 shows the location of turbine within the computational domain. The turbine rotational plane is located $4R$ away from the inlet and the fluid
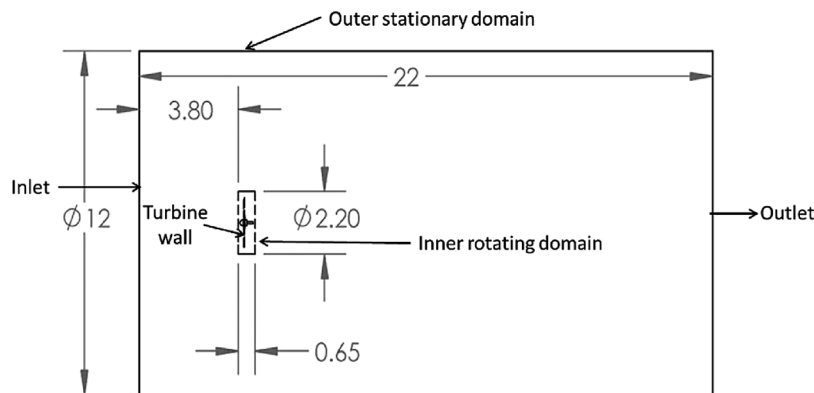
FIG. 2. Computation domain, used for CFD analysis.

domain extends *18R* behind the turbine rotational plane to capture the near wake and far wake effects. The inlet boundary condition was applied on the east face of the domain with uniform axial (free-stream) velocity (U) of 2 m/s with V and $W = 0$ and turbulence intensity of 10%. A high resolution (bounded second-order upwind biased) discretization scheme was used for advection and turbulence. The convergence criteria for rms residuals were set to 10^{-6} for continuity, momentum, and turbulence quantities. All the domains were initialized with the initial velocity of $U = 2$ m/s. The CFD simulations presented in this paper are steady state calculations performed using a multiple reference frames technique; details about this technique can be found elsewhere,[25] which was validated and published in Ref. 25. A rotating reference frame was incorporated to take into account the effect of the turbine rotation by transforming an unsteady flow in an inertial (stationary) frame to a steady flow in a non-inertial (moving) frame using Eqs. (6) through (8). The CFD study consisted of HKTs rotating at various rotational speeds 40 rpm to 135 rpm which corresponds to the TSR range of 2 to 7. The mesh used for current CFD study is an unstructured mesh with very fine prism layers near the turbine wall. A grid independence study was carried out to study the effect of the number of elements on the CFD analysis. Mesh size was varied from a coarser mesh of 3.5×10^6 to a finer mesh of 10×10^6 elements and flow variables were monitored. As the mesh size is increases, turbine power increases and stabilizes around 7.8×10^6 elements. The percent change in output power from 7.8×10^6 element grid to next coarser grid (6.6×10^6 cells) was 1.3%. Hence a mesh with 7.8×10^6 elements was found optimal from the accuracy and the computational expense standpoint and used for current CFD study. In addition to the global mesh size study, a convergence study on the global converged mesh was performed to understand the effect of y^+ value on the turbine power and thrust prediction. This study consisted of locally refining the near wall prism layers to reduce the y^+ value. For the global converged mesh, the thrust and power values started to converge around the y^+ value of 100. Hence considering the computational expense and accuracy, the final computational grids used during the current CFD study consisted of the meshes with y^+ value of less than 100 for the converged performance characteristics. The height of the first prism layer on the turbine wall was set such that the grid elements adjacent to the turbine wall were within the logarithmic region of boundary layer with a y^+ values between 30 and 100. A y^+ value is a non-dimensional parameter related to mesh size which defines distance of first mesh node from the wall. Lower the y^+, better the boundary layer flow resolved near the wall.[53] Convergence criteria for the continuity and momentum equations were set to 10^{-6} absolute and higher order numerics were used for turbulence modeling.

2. Structural dynamics equations:

The conservation of momentum equation of a solid continuum in a Lagrangian framework can be expressed as

$$\rho_s \frac{\partial^2 \delta_s}{\partial t^2} - \nabla \cdot \tau_s = f_s, \tag{9}$$

where ρ_s represents structural density, f_s represents body force vector per unit volume on the structure, δ_s represents structural displacement field, and τ_s is a symmetric Cauchy stress tensor. In the present analysis, the fluid flow equations are solved to find the resultant forces on

FIG. 3. Finite element mesh used for structural solver.
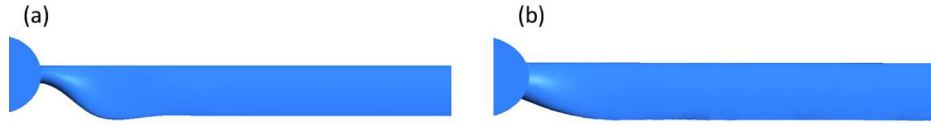
FIG. 4. Blade shapes used for FSI analysis: (a) circular blade root and (b) parabolic blade root.

interface and then stresses are calculated by solving the structural equations. Thus the kinematic condition for no slip interface can be rewritten as

$$\delta_f = \delta_s, \tag{10}$$

where δ_f is the fluid displacement. This forms the displacement boundary condition for fluid-structure interface. The dynamic condition for the fluid-structure interface requires that the fluid and structural stresses be in equilibrium

$$n_f.\tau_f = -n_s.\tau_s, \tag{11}$$

where n is a unit normal vector pointing outward from the respective domains. The Dirichlet-Neumann formulation of FSI presented in Eqs. (10) and (11) implies that the fluid flow equations are solved for the fluid-structure interface velocity and stresses are imposed on fluid structure boundary of solid domain.[32,33,45] Figure 3 shows the mesh used for FEA which consists of around 1×10^5 elements. In an effort to understand the effect of blade root section on the turbine stresses, two different blade geometries were modeled (Figure 4). The main difference in these geometries is at the root section where blade mates with turbine hub; this section is circular for geometry-I (Figure 4(a)) while it is parabolic for geometry-II (Figure 4(b)).

III. RESULTS

A. BEM validation

The BEM code was validated with NREL phase III combined experimental rotor (CER) results,[54] primarily due to absence of detailed experimental data for HKTs. The NREL CER
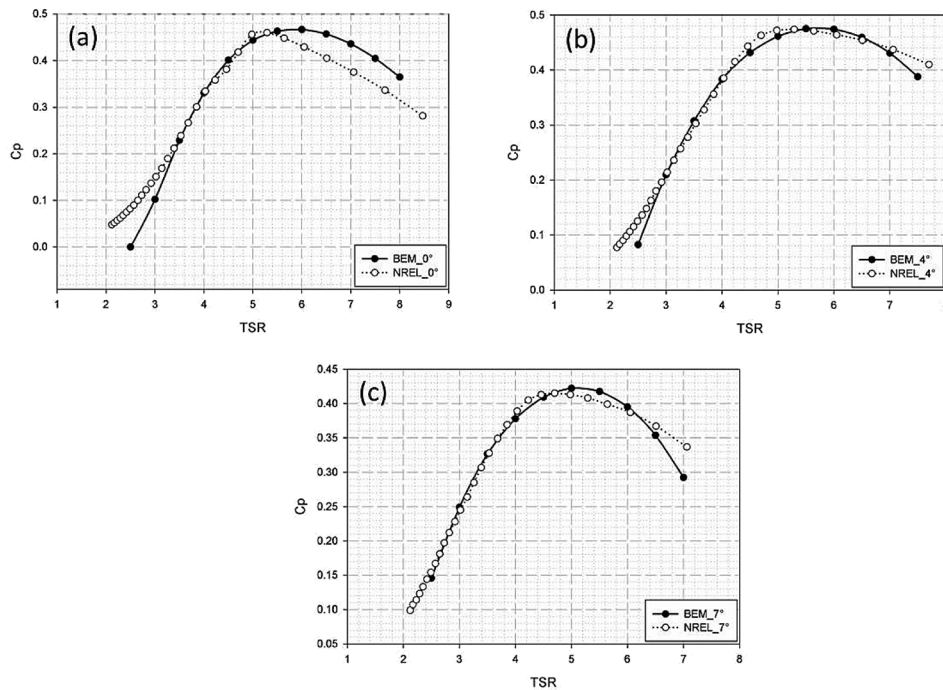
FIG. 5. Validation of BEM with NREL experiments: (a) 0° blade pitch, (b) 4° blade pitch, and (c) 7° blade pitch.
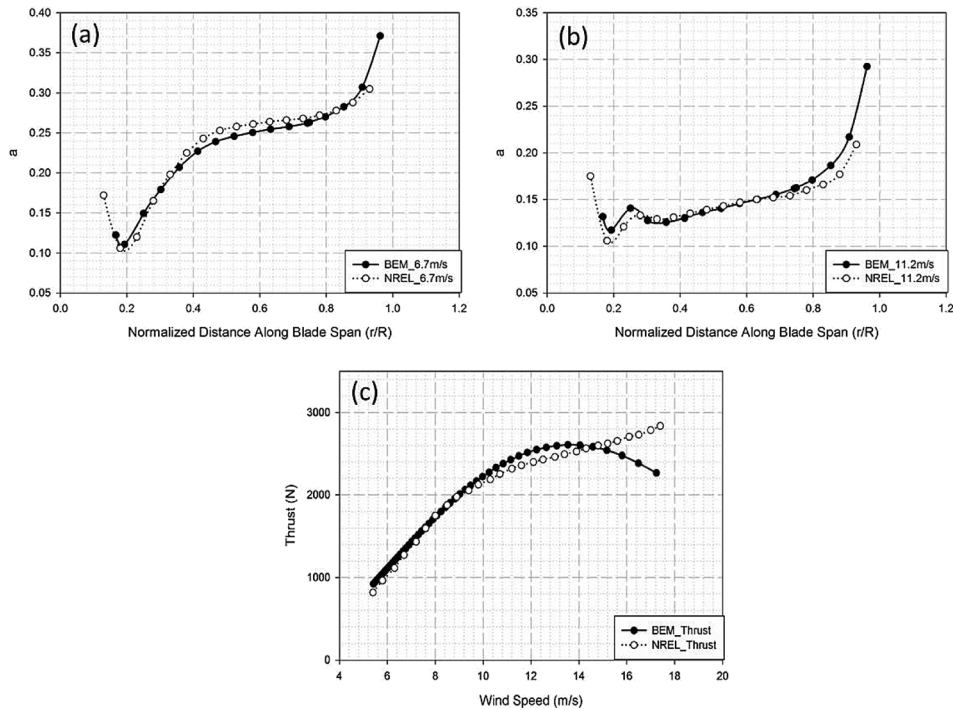
FIG. 6. Comparison of BEM analysis with NREL experimental data: (a), (b) axial induction factor and c) thrust forces.

rotor is a 5.03 m radius stall regulated downwind turbine with a rated power of 20 kW that has varying chord and twisted blades. This turbine uses S809 airfoil from blade root to tip with a chord and twist distribution along blade span.[54] Experimental data is available[54] for two and three bladed turbine configurations at constant rotational speeds of 72 and 83 rpm at various blade pitch angles. A BEM analysis was carried out for a rotational speed of 72 rpm for the three bladed turbine over a range of blade pitch angles (0° to 7°) and TSR (0 to 8). Figure 5 compares C_p from BEM analysis with the NREL data, which shows a good match up to TSR of 5. At high TSR values, BEM analysis deviates from the experimental data which can be attributed to a non-uniform blade loading[55] and accelerated span-wise flow effects that are not taken into account in one-dimensional momentum analysis. BEM does not consider the hydrodynamic interaction between the adjacent blade elements and large out of plane deflections at higher TSR introduces errors in hydrodynamics modelling as BEM essentially assumes that the momentum is balanced in a plane parallel to the rotor. Figures 6(a) and 6(b) compare the axial induction factors (*a*) along the blade span at 6.7 m/s and 11.2 m/s wind speeds, respectively. The BEM analysis results follow similar trend as the NREL experiments results, but, in general, the axial induction factors computed from BEM are smaller than those obtained from the experimental data. Figure 6(c) plots the thrust forces exerted on a turbine blade as a function of wind speed. Results of BEM are comparable with the experimental data till wind speed of 14 m/s, but at higher speeds, 1D BEM analysis deviates from the experimental data due to high flap-wise loading and out of plane deformation which cannot be captured accurately by the momentum theory of BEM method.

B. Analysis for a constant chord zero twist blade turbine

1. BEM parametric study

After validating the mathematical model, a parametric study based on BEM theory with the necessary corrections (Prandtl's tip loss correction, hub loss correction, corrections for Reynolds number effect on hydrodynamic data) was performed for a model three-bladed constant chord

TABLE I. Design variables for BEM parametric study of hydrokinetic turbines.

Design variable	Value/range
Number of blades (B)	3
Turbine radius (R)	1 m
Hub radius (r_{hub})	0.085 m
Number of blade elements (N)	20
Water velocity (U)	2 m/s
TSR	2–12
Chord length (c)	0.015–0.18 m
Blade pitch angle (θ_{po})	0°–18°

turbine ($R = 1$ m). A SG6043 profile was chosen from root to tip as it gives a high C_L/C_d value over the current operating range of Reynolds numbers ($1 \times 10^5 < Re < 5 \times 10^5$). Table I summarizes various parameters studied during the current analysis. BEM analysis is performed to understand the effect of chord length, blade pitch (θ_{po}) and TSR on the performance of the turbine. The turbine blade was divided into 20 blade elements and BEM analysis was performed to find the thrust forces and the torque developed on the turbine blades according to Eq. (3). The water velocity used for this analysis was 2 m/s which is the upper limit of observed river water velocity for large sinuous canaliform rivers like the Mississippi and Missouri rivers.[56] The design TSR is varied from 2 to 12, blade pitch angle from 0° to 18° and chord length from 0.015 to 0.18 m. Figure 7 shows the effect of blade pitch, TSR and chord on the performance coefficient. As the chord length is increased from 0.03 to 0.12 m as plotted in Figures 7(a)–7(c); the bell shaped curve of C_p plotted against TSR moves towards the origin, which indicates that higher the chord length, lower the TSR for optimum performance. Also, for a given chord length, lower the TSR, higher the blade pitch for maximum performance. A higher θ_{po} means higher angle of attack of incoming fluid which results in higher
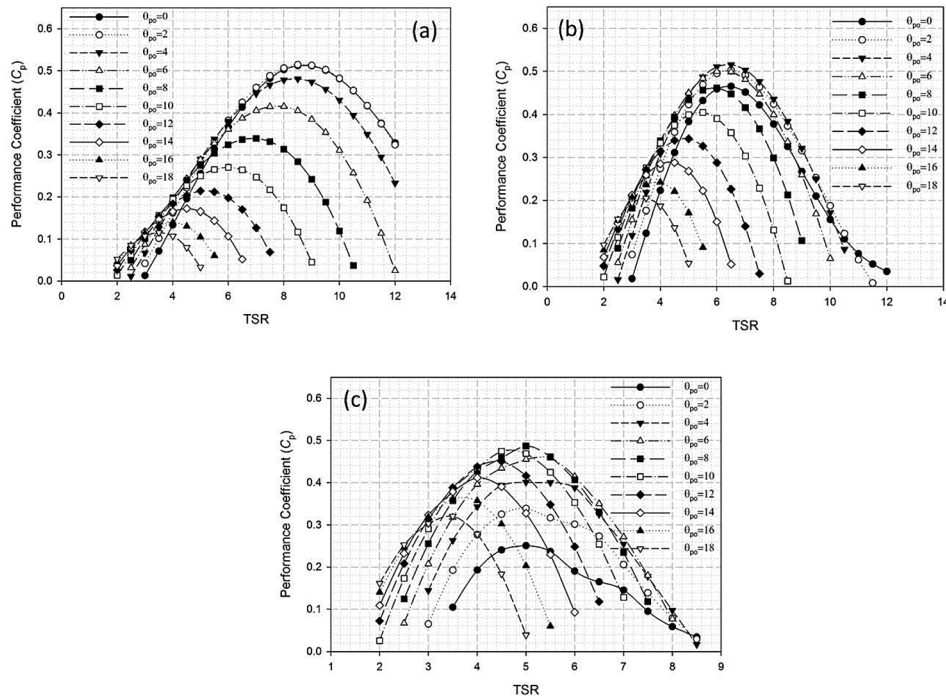
FIG. 7. Effect of TSR and blade pitch angle on turbine performance at various chord lengths: (a) 0.03 m chord, (b) 0.06 m chord, and (c) 0.12 m chord.

lift forces (hence torque) on turbine blades. This results in lower rotational speeds and hence lower TSRs for optimum hydrodynamic performance with increasing θ_{po} values. For higher chord length blades (0.06 m and 0.12 m), an increase in θ_{po} results in higher C_p till a critical θ_{po} is reached for corresponding chord lengths. For $c = 0.06$ m chord blade, maximum C_p is observed at $\theta_{po} = 4°$ (TSR = 6.5) and for $c = 0.12$ m, maximum C_p is observed at $\theta_{po} = 8°$ (TSR = 5) (Figure 7). This can be attributed to higher lift forces acting on blade surface with increasing angle of attack till it reaches a stall angle after which a reduced performance is observed. For the low solidity blade ($c = 0.03$ m), maximum performance was observed at $\theta_{po} = 0°$, and TSR = 8.7. An increase in θ_{po} resulted in lowering the TSR for maximum C_p similar to 0.06 m and 0.12 m chord blades, but this was accompanied by a reduction in maximum achievable C_p as well. Thus for a low solidity blade, an increase in angle of attack did not produce higher power but only resulted in lowering the operational TSR range.

Figure 8 shows the effect of chord length, TSR, and blade pitch on stresses developed in turbine blades. This analysis assumes blades to be fixed at the rotor hub as a cantilever beams and stresses are computed based on the thrust force exerted on rotating blades due to flowing fluid. From Figure 8, it is evident that the chord length and hence blade thickness has a significant role in reducing the stresses and improving the strength of the turbine blades. For a given chord length, stresses in a turbine blade depends not only on the total thrust force but also its distribution along the blade span. Such a distribution is a function of blade TSR, pitch angle, blade airfoil, and blade root geometry. As expected, the stresses are higher at higher TSR and lower pitch angle values due to higher rotational speeds (high TSRs) and higher drag forces due to larger projected blade area exposed to flow (low blade pitch angles). For a chord length of 0.03 m, the stresses in turbine blade continue to increase with TSR for all blade pitch angles. Due to a smaller chord length (hence thinner blade), the flap-wise bending stresses are very high for all TSR values, thus making this design structurally unsafe. As the chord length increases from 0.03 m to 0.06 m and 0.12 m, the turbine blade becomes structurally more stable. At these higher chord lengths, with increasing TSR, stresses first increase and then decrease after a critical TSR for each blade pitch angle is reached. Moreover, it was observed that the
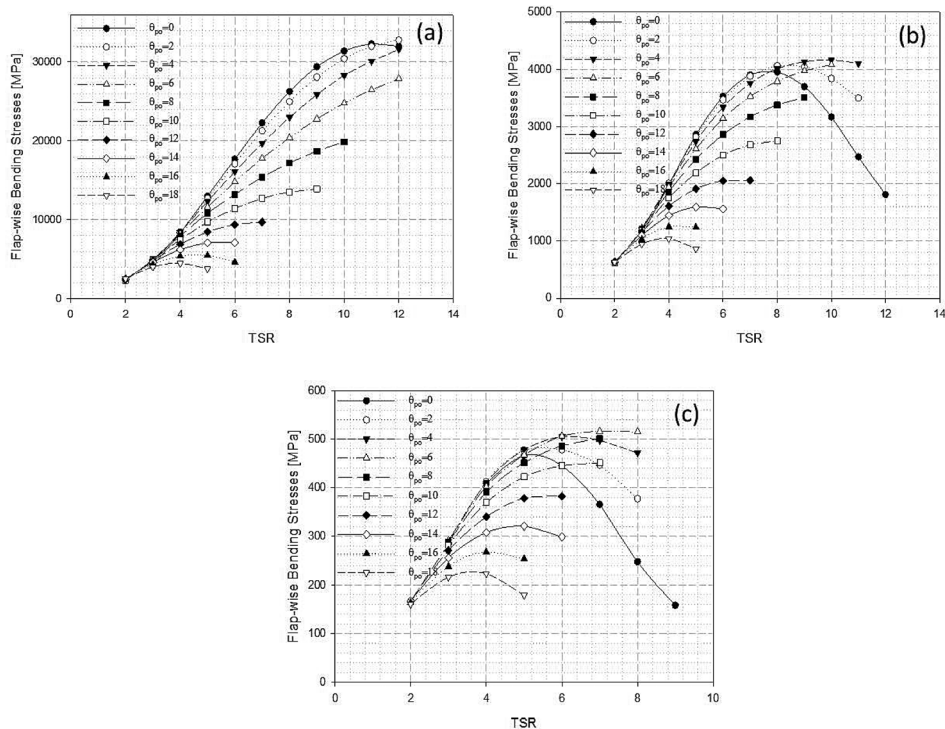
FIG. 8. Effect of design variables on flap-wise bending stresses: (a) 0.03 m chord, (b) 0.06 m chord, and (c) 0.12 m chord.

blade pitch angle for maximum stress is different for different chord-lengths: for $c = 0.03$ m, the maximum stress was observed at $\theta_{po} = 14°$, for $c = 0.06$ m at $\theta_{po} = 4°$ and for $c = 0.12$ m at $\theta_{po} = 6°$. This illustrates the complex nature of stress and its dependence on TSR and c, and θ_{po}. Our parametric study based solely on the hydrodynamic analysis suggests that lower values of blade pitch angles and chord lengths maximize the coefficient of performance, while the structural analysis suggests that higher blade pitch angles and lower TSR are required for the structural stability of turbine. A trade-off between efficiency and structural strength is thus important for an efficient HKTs design that was achieved using multi-objective optimization with GA. The results from parametric study were used to specify bounds on the chord length, TSR, and blade pitch angle for optimization.

2. Multi-objective optimization: Genetic algorithm

GA is a heuristic search and optimization technique which converges to a global minimum by searching over a population of possible solutions. Unlike traditional optimization methods like gradient search and simplex methods, GA requires information about fitness function only and not its derivatives.[57] Figure 9 illustrates a flow diagram of the procedure adopted in this work. GA is based on a natural selection process that mimics biological evolution and iteratively modifies a population of individual solutions.[58,59] Individuals from the current population are used as parents to produce the children for the next generation. Over successive generations, the population *evolves* toward an optimal solution. The output from GA is a set of multiple possible solutions (Pareto optimal solution set), so designer has a choice to choose the best feasible solution as per his requirements. A multi-objective optimization was developed using MATLAB. The problem consists of finding a set of decision variables: blade pitch, TSR, and chord length which optimizes C_p and thrust forces. The objective function $F(x)$ is defined as
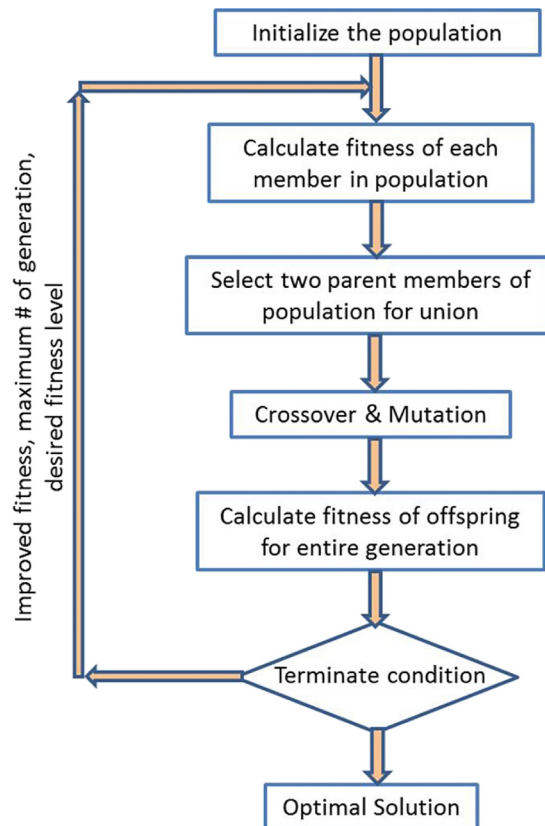
FIG. 9. Flowchart for genetic algorithm based multi-objective optimization.

$$F(x) = [f_1(x), f_2(x)], \quad \text{where} \quad f_1(x) = -C_\mathrm{p}(\theta_{po}, \text{TSR}, c), \quad f_2(x) = +T(\theta_{po}, \text{TSR}, c). \quad (12)$$

GA algorithm is designed to minimize both $f_1(x)$ and $f_2(x)$; the negative sign on C_p and positive sign on T ensure that both hydrodynamic and structural performances are maximized. The design space selected for the current study is such that TSR is varied from [2, 6], blade pitch angle from [8°, 16°] and chord length from [0.08 m, 0.18 m]. The experience gained from a wind turbine literature is used to specify TSR range for the parametric study.[55,60] For a wind turbine, which is a lift-drag device similar to HKTs, the TSR for maximum C_p ranges from [6, 10]. For HKTs, the average river water speed is ~2 m/s while the average rated operating wind speed for wind turbine is ~13 m/s. Since water is almost 800 times denser than air, HKTs should be designed and optimized such that the operational range of TSR is below that of the conventional wind powered machines. Hence the design TSR space for this study is chosen as in [2, 6]. The SG6043 hydrofoil used for the current study has stall angle around 14°–16° over the operational range of flow Reynolds number ($1 \times 10^5 < Re < 5 \times 10^5$). Hence, a pitch angle range of [8°, 16°] is expected to cover all possible optimal operating blade pitch angles for optimizing C_p. The maximum chord length was restricted to 0.18 m which corresponds to R/c of 0.56 ($\sigma = 0.086$). Higher the chord length, larger the blade area undergoing thrust loading (and higher the inertia) which is detrimental to the turbine life. Further, an increase in chord length does not improve the performance significantly but only lowers the TSR for maximum performance.[13,24] The results of GA optimization are shown in Figure 10 which plots a Pareto curve obtained from GA algorithm. The multi-objective optimization based GA algorithm minimizes the structural stresses and a negative value of C_p as defined in our objective function. Each point on this curve represents a feasible optimized solution ($-C_\mathrm{p}$, stress) with optimal design variables (chord-length, TSR, and blade pitch angle). It was observed that, higher the C_p, higher the stresses, hence a higher C_p can be attained for stronger blade material with high allowable stresses. Table II presents sample solutions from Pareto optimal solutions space. The stresses presented in Table II are flap-wise bending stresses in turbine blades calculated based on thrust forces and blade size at root and determined according to Eq. (5). Incorporation of this simple analytical form for stresses in BEM analysis made it possible to perform a multi-objective optimization analysis. The turbine performance improves with increasing TSR and decreasing chord-length but at the cost of higher stresses. With increasing TSR, a decrease in blade pitch angle is observed for maximum performance which is consistent with BEM
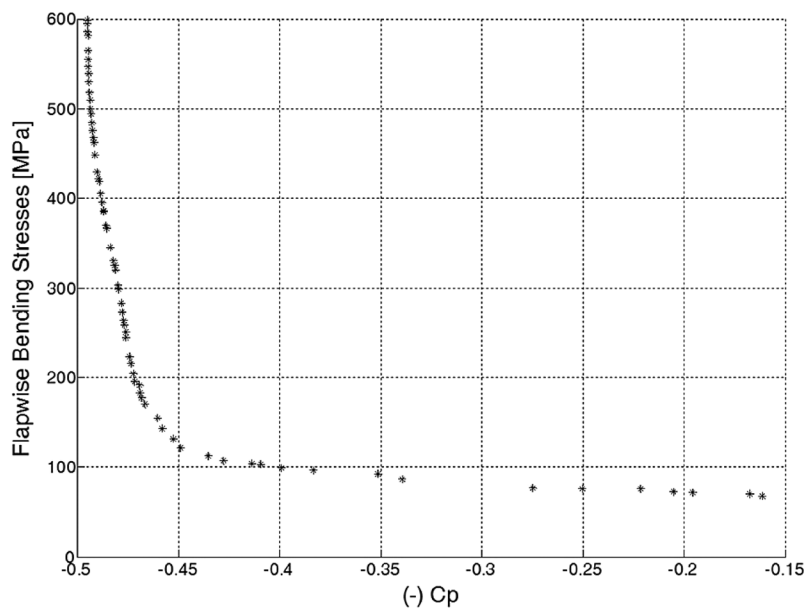
FIG. 10. Pareto optimal curve from GA multiobjective optimization.

TABLE II. Optimal solutions obtained from GA multiobjective optimization for a constant chord blade.

Sr. #	Blade pitch (°)	TSR	Chord (m)	Cp	Stress (MPa)
1	14.32	3.48	0.18	0.44	108
2	12.57	4.22	0.18	0.45	129
3	11.69	4.40	0.17	0.46	145
4	10.39	3.72	0.16	0.47	177
5	10.33	4.58	0.15	0.47	210
6	10.18	4.61	0.15	0.48	243
7	9.58	4.76	0.14	0.48	276
8	9.15	4.78	0.14	0.48	300

parametric study. A detailed coupled CFD-FEA analysis was performed later to validate the results of optimization and check the fidelity of our lower order BEM technique and is described in Sec. III B 3.

3. FSI analysis

A fluid structure interaction analysis is carried out using a partitioned one-way coupling. CFD analysis was performed in ANSYS CFX where fluid domain equations were solved in a rotating reference frame technique to find torque and thrust forces on turbine blades. The fluid solver is coupled with the structural solver and fluid forces obtained from CFD are then transferred to the structural domain at fluid structure interface. Finite element analysis was carried out in ANSYS Mechanical. Figure 3 shows the mesh used for FEA which consists of around 1×10^5 elements. More than 99.5% of nodes were mapped at the fluid structure interface for all cases. The blade material used for FE analysis was a structural steel with density $(\rho_s) = 7850 \, \text{kg/m}^3$; Yield strength $(\sigma_{yt}) = 280 \, \text{MPa}$ and ultimate strength $(\sigma_{ut}) = 460 \, \text{MPa}$.

Table III compares the results of CFD analysis to forces and Cp obtained from BEM calculations. The data is presented for 10°, 10.39°, 12°, 13.5°, and 14.4° blade pitch angle cases at different TSR and chord lengths, which are Pareto optimal solutions from GA. The coefficient of performance and force values obtained from CFD analysis are comparable to those obtained from BEM analysis. It was found that even though the torque and thrust forces from BEM analysis was in agreement with our CFD analysis, stress values deviate from those determined with detailed FEA. The pressure field on the turbine blades (and hence the stress field) is complex due to combination of thrust, centrifugal, and Coriolis forces acting on the blades. These forces were not precisely addressed in a BEM based theory. The stresses in turbine blades depend not only on the magnitude of thrust forces on the blade but also on its distribution along the blade

TABLE III. Summary of FSI and BEM analysis.

	Variables				CFD	FEA				BEM		
Geometry	Blade pitch (°)	Chord (m)	TSR	Cp	Thrust (N)	Flap-wise stress (Mpa)	von-Mises stress (Mpa)	Stream-wise deflection (cm)	Microstrain	Cp	Thrust (N)	Flap-wise stress (Mpa)
I	10	0.12	4	0.45	4753	282	364	4.7	1890	0.42	4832	372
I	10	0.12	3	0.36	3835	240	312	3.9	1616	0.29	3613	278
I	12	0.12	4	0.42	4241	298	340	4.5	1762	0.43	4403	339
II	10.39	0.16	3.72	0.47	5449	215	210	2.4	1050	0.4	5211	179
II	10.39	0.16	4.56	0.46	5678	209	208	2.3	1046	0.47	5823	189
II	13.5	0.14	3.12	0.35	3627	253	332	2.5	1663	0.36	3881	188
II	14.4	0.14	3.52	0.38	3817	263	345	2.7	1725	0.39	4121	200
III	10.39	0.16	3.72	0.47	5254	196	200	1.7	1009	0.4	5211	179
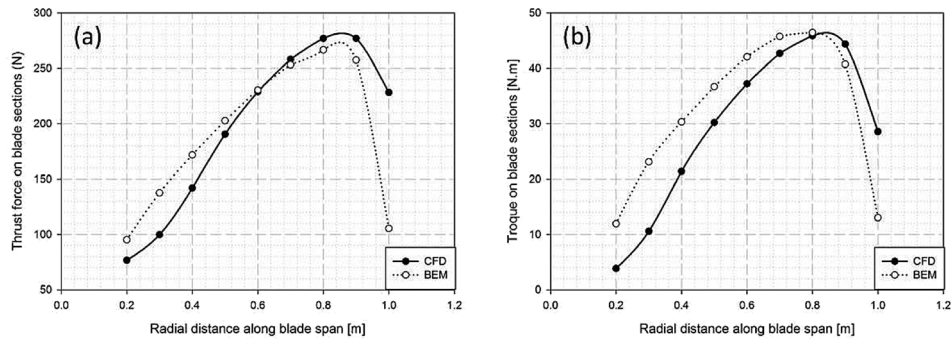
FIG. 11. Comparison of BEM with CFD for 10.39° pitch, 3.72TSR and 0.16 m chord blade HKT (a) Thrust force and (b) torque distribution along the blade span.

span and CFD analysis determines the detailed pressure/force field on blades. This distribution along the spanwise direction is transferred to the structural solver for stress calculations as opposed to thrust forces calculated on distributed blade elements in BEM analysis. Table III compares the stresses obtained from FEA with those from BEM analysis. For $c = 0.12$ and $\theta_{po} = 10°$, increase in TSR from 3 to 4 results in increased C_p at the cost of higher stresses. For higher chord length ($c = 0.16$ m), the TSR was observed not to have a significant effect on C_p. With increased TSR, though the thrust force on blade increases, the thicker blade section results in lower stress values which can be seen in Table III. Comparison of case 1 to case 3 in Table III shows that an increase in θ_{po} from 10° to 12° for the same TSR and c values resulted in reduction in performance coefficient with almost similar stress values. Figure 11 plots thrust and torque distribution over the blade span obtained from BEM and CFD analysis for a 10.39° pitch, 3.72TSR and 0.16 m chord blade turbine case. For the near tip and near hub region, the BEM analysis deviates from CFD results as it does not take into account the effects of three dimensional flow and vortices formed at these regions. Furthermore, this corresponds to a deviation in stress predicted from BEM compared to FSI analysis. It should be noted that the stresses determined from BEM are based on area moment of inertia of blade hydrofoil cross-section near blade root and does not take into account the effect of geometry of blade particularly at blade root where blade cross-section changes form airfoil to a circular shape (Figure 4). The results from CFD analysis for similar turbines operating under same operating conditions but different blade root sections supports this hypothesis. Figure 4(a) shows the blade geometry-I used for cases 1–3 in Table III; and for all other cases 4–8, geometry-II similar to Figure 4(b) was used. The main difference in the geometry is at the root section where blade mates with turbine hub; this section is circular for geometry-I while it is parabolic for geometry-II. The circular cross-section of geometry-I was found to be structurally stronger than parabolic section of geometry II resulting in lower flap-wise stresses when compared to stresses obtained from BEM. It was also observed that maximum von-Mises stress occurs at the transition region where blade cross-section changes from airfoil to parabolic/circular. Figure 12(a) shows the von-Mises stress distribution on turbine for case 4 ($\theta_{po} = 10.39°$, $c = 0.16$ m, TSR = 3.72) in Table III which clearly shows maximum stress of 211 MPa in the transition region. Figures 12(b)–12(d) show span-wise distribution of von-Mises stresses on pressure side of blade at 25%, 50%, and 75% of chord measured from trailing edge, where maximum stress is observed near the leading edge side of blade. Table III also summarizes strains and deflection of turbine blades at various optimal operating conditions obtained from GA optimization analysis. Coefficient of performance as high as 0.47 can be obtained with stream-wise blade deflection of 2.4 cm (2.4% of R) and 1050 microstrains (cases 4 and 5 in Table III). Case# 8 illustrates the effect of size of blade root section on the induced stresses in turbine blade. The operating conditions and blade geometry of case 8 (geometry-III) were exactly similar to case 4, but the minor diameter in the transition region was increased by 20% which resulted in 5% reduction in stresses without affecting the hydrodynamic performance of the turbine.
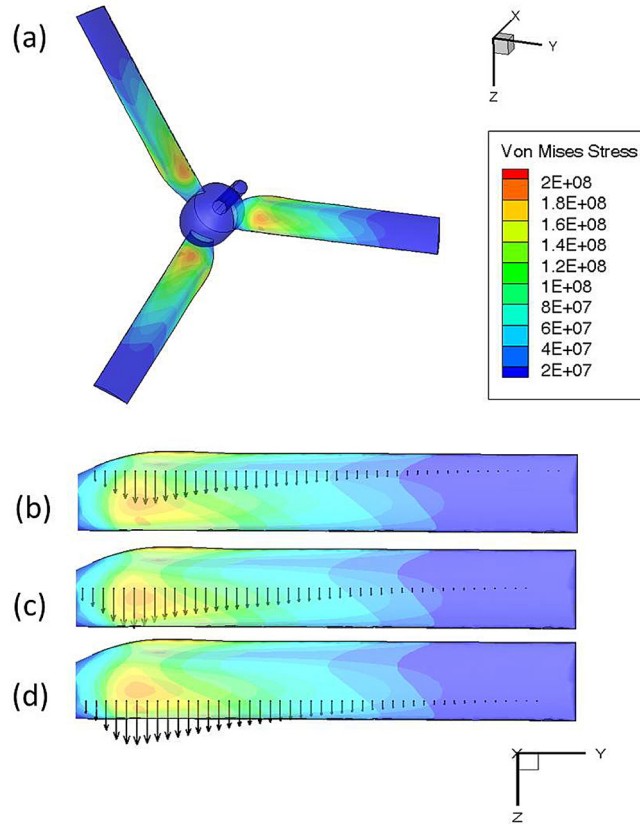
FIG. 12. von-Mises stress distribution for 10.39° pitch, 3.72TSR and 0.16 m chord blades HKT: (a) Contour plots of von-Mises stress on complete turbine; Vectors of von-Mises stress at (b) 25% chord, (c) 50% chord, and (d) 75% chord, all measured from trailing edge.

Figure 13 plots the streamlines of velocity in stationary reference frame on upwind and downwind side of the turbine blade (for case#4 in Table III) which shows swirling effect near hub responsible for hub loss effect. Further the suction side of the blade shows presence of laminar separation bubble and flow reattachment. This was due to the fact that SG6043 hydrofoil that was used for current analysis exhibits laminar separation bubble formation at Reynolds number of $\sim 1 \times 10^5$.[12,61,62] The operating Reynolds number for this case (case#4 in Table III) is $\sim 3 \times 10^5$ which is higher than the laminar separation bubble Reynolds number for SG6043. The flow reattachment behind laminar separation bubble and finally turbulent separation occurs at this high Reynolds number. This results in a delayed separation to higher stall angles and increased lift forces on turbine blades. The effects of these phenomena on the turbine performance and loading were not addressed in BEM analysis but precisely captured in three-dimensional CFD analysis. Figure 14 plots contours of total pressure in stationary frame of reference at various span-wise locations (0.2R, 0.45R, 0.75R, and 0.99R) which shows variation of angle of attack along the blade span, highest being near the blade root (Figure 14(a)) and decreasing progressively towards blade tip (Figure 14(d)). This angle of attack is indicative of lift and drag forces generated by blade at various sections and can be used as an effective tool for defining blade twist along blade span to maximize turbine performance and reduce structural loads. Figure 15 shows contours of non-dimensional total pressure ($P_{total}/\rho U^2$) in stationary reference frame on upwind and downwind side of the turbine blade. The part of turbine blade near tip experiences higher non-dimensional total pressure on pressure side of blade and lower non-dimensional total pressure on suction side of blade compared to the rest of the blade. A higher ΔP across the blade section is indicative of higher structural loading. This uneven loading not only reduces the turbine performance but also detrimental to the turbine life. To

FIG. 13. Streamlines of velocity in stationary reference frame on (a) upwind side and (b) downwind side of the turbine blade.

reduce the structural loading on the turbine blade and achieve more uniform loading, a multi-objective optimization was carried out by applying twist and chord distribution to the blade geometry and is discussed next.

C. Analysis for a varying chord and twisted blade turbine

1. Hydrodynamic optimization and parametric study

Higher stress values were observed near the blade root section for an optimized constant chord blade turbine. In addition, CFD analysis for optimized constant chord design indicated a possibility of improvement in hydrodynamic and structural performance of turbine. Hydrodynamic optimization was thus carried out to study the effect of chord and twist
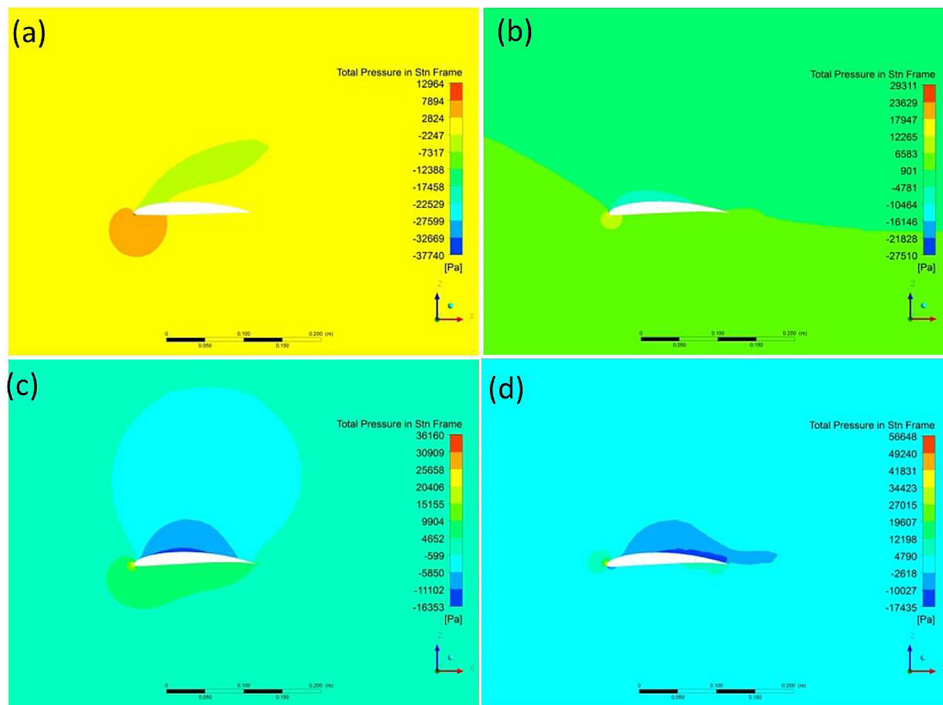
FIG. 14. Contours of total pressure in stationary frame on planes at (a) 0.2R, (b) 0.45R, (c) 0.75R, and (d) 0.99R blade span.
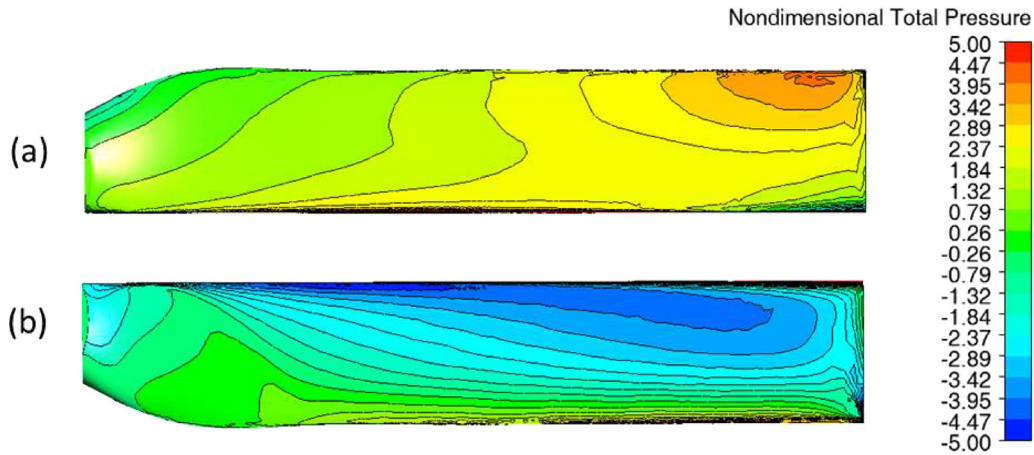
FIG. 15. Contours of non-dimensional total pressure ($P_{\text{total}}/\rho U^2$) in stationary reference frame on (a) upwind side and (b) downwind side of the turbine blade.

distribution on the turbine performance. The optimization was performed considering the effect of wake rotation for different design (rotational) speeds.[63] The design speeds chosen for this analysis were 75 rpm (Design_N75), 100 rpm (Design_N100), and 125 rpm (Design_N125) which corresponds to a design TSR of 3.93, 5.24, and 6.55, respectively. All these designs assume a water velocity of 2 m/s and a design blade pitch angle (θ_{po}) of 0°. Figure 16(a) shows the chord length variation along the blade span. For all three designs, the chord length is higher near the hub and progressively decreases towards the blade tip. Figure 16(b) compares the twist distribution along the blade span for all three designs. For optimum performance, the blade twist (θ_t) at any blade section depends on local tip speed ratio (TSR-λ) which in turn depends on the design tip speed ratio (TSR-λ_d) and radial distance (r) of the blade element from the axis of rotation. The design for faster rotating turbine (Design_N125) has lower twist angles and smaller chord length along the blade span compared to other designs due to lower angle of relative wind. Equations (13)–(15) illustrate the dependence of ϕ and θ_t on λ_d, r, R, blade pitch angle and angle of attack (α)

$$\lambda_d = \frac{R\Omega}{U}; \quad \lambda = \frac{r}{R}\lambda_d,$$
(13)

$$\theta_t = \tan^{-1}\left(\frac{2}{3\lambda_r}\right),$$
(14)

$$\phi = \theta_{po} + \theta_t + \alpha.$$
(15)
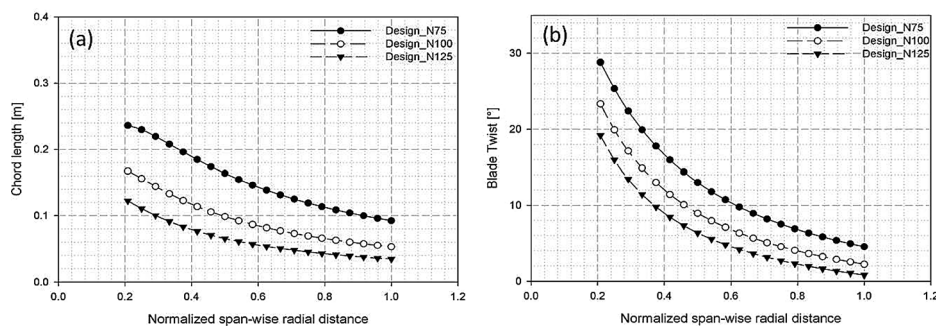
FIG. 16. Comparison of various blade designs showing (a) chord distribution and (b) twist distribution along blade span.
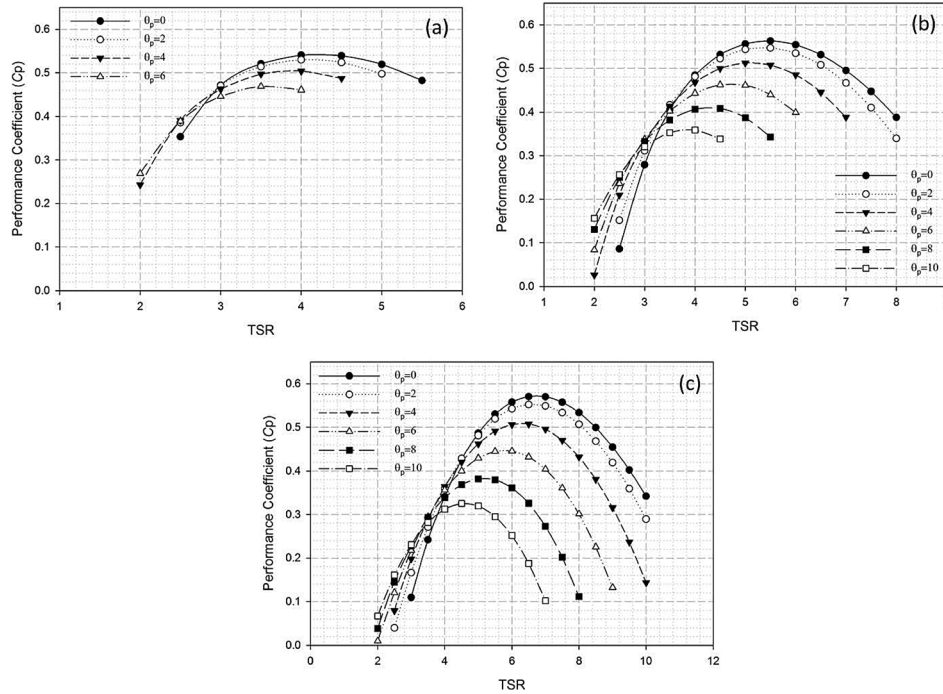
FIG. 17. Effect of TSR(λ) and blade pitch angle on performance coefficient for (a) Design_N75, (b) Design_N100, and (c) Design_N125.

Figure 17(a) shows the effect of TSR on C_p at various blade pitch angles for Design_N75. This blade was designed for rotational speed of 75 rpm (TSR = 3.93), blade pitch angle of 0° and attains maximum performance of 0.54 at these design values. A reduction in performance is observed with increasing blade pitch angles. Further, increasing a blade pitch angle reduces the TSR for maximum performance. Figure 17(b) plots C_p against TSR for various blade pitch angles of Design_N100. This blade is designed for rpm of 100 (TSR = 5.24) and blade pitch angle of 0° and gives C_p of 0.56 at these design conditions. Similar to Design_N75, this blade configuration also shows reduction in performance as blade pitch deviates from design value of 0°. Figure 17(c) shows effect of TSR and blade pitch angle on C_p of design for 125 rpm. A reduction in performance is observed as we move away from design rpm of 125 (TSR = 6.55) and blade pitch of 0°. The Design_N125 was observed to be less susceptible to the variation in design values and performs better over a wider range of TSR and blade pitch angles.

2. Multi-objective optimization with GA

It can be noted that the chord and twist distribution for all three hydrodynamically optimized designs follow a similar trend (Figures 16(a) and 16(b)). Hence curve fits to chord and twist distribution of Design_N100 were used for the multi-objective hydro-structural optimization. The near hub chord-lengths were varied in the range [0.16 m, 0.10 m] and near tip chord-lengths in the range [0.05 m, 0.03 m] for GA optimization. As these designs were hydrodynamically optimized for blade pitch of 0°, for GA multi-objective optimization, the design space for blade pitch was set to [−3°, 3°] and TSR to [2, 7] to cover design TSRs of all three designs. Table IV presents representative Pareto optimal solutions obtained from GA for variable chord, twisted blade geometry. As compared to a constant chord design (Table II), this design yields higher C_p and lower stresses in the turbine blades. The C_p is improved from 0.47 (for constant chord blade design) to 0.55 (for variable chord, twisted blade design) with flap-wise bending stresses below 200 MPa. This can be attributed to a more uniform blade loading by virtue of providing a variable chord and twist distribution to the blade. Moreover, during

TABLE IV. Pareto optimal solutions from GA for variable chord twisted blade.

Sr #	Pitch [°]	TSR	Cp	Flap-wise bending stress [Mpa]
1	1.46	3.68	0.39	103.5
2	1.48	3.91	0.42	111.6
3	1.52	4.22	0.45	121.4
4	1.44	4.55	0.48	131.7
5	0.87	4.82	0.51	140.8
6	1.05	5.21	0.52	148.8
7	0.07	5.40	0.53	158.6
8	0.02	5.72	0.54	165.2
9	−0.48	5.42	0.54	161.4
10	−0.92	5.87	0.54	174.0
11	−1.15	5.99	0.55	199.0

CFD analysis for a constant chord blade, it was observed that the larger near tip area of a constant chord design was responsible for higher thrust force which resulted in higher bending moment and hence higher stresses in the turbine blade. A variable chord twisted blade design results in reduced stresses and improved hydrodynamic performance due to higher blade twist near hub region and smaller chord-length (hence blade area) near blade tip. Thus a variable chord, twisted blade design performs better than a constant chord blade from both a hydrodynamic and structural sense.

IV. CONCLUSION

A multi-objective hydro-structural optimization was presented for both constant chord, zero twist blade turbine, and variable chord, twisted blade turbine designs. GA based on BEM proved to be a fast and efficient tool for hydro-structural optimization of HKTs. The results of optimization for a constant chord, zero twist blade design were supported with detailed CFD and FE analysis. Compared to the CFD analysis, the thrust and torque loading calculated from BEM are under-predicted near the blade tip and over-predicted elsewhere. But the integral performance parameters (total thrust and torque) calculated from BEM agree well the CFD analysis. The total thrust forces obtained from the BEM analysis were comparable to the FSI analysis within ∼7% variation. Thus the BEM analysis offered a quick, reliable tool for multi-objective optimization which would have been virtually impossible with CFD analysis due to higher computational time involved. Though the BEM analysis was able to predict the total thrust and torque loading on a turbine, it could not capture the variation of these forces along the blade span due to inherent simplifications of the BEM theory. On the other hand, coupled CFD-FE analysis precisely determined this force distribution along the blade span and also considered the effect of blade root thickness. This resulted in larger deviation (up to 30%) between stress compared to forces calculated from BEM and FSI analysis. A variable chord, twisted blade turbine was found to improve structural performance of turbine without compromising any of the hydrodynamic efficiency. Three different blade designs were presented for different rotational speeds and optimization was performed for variable chord, twisted blade design for hydro-structural performance improvement. The significant findings from our analysis are summarized below

- Lower values of blade pitch angles and chord lengths maximize the hydrodynamic performance while for the structural stability of turbine, a higher blade pitch angle, and lower TSR are required
- A hydro-structural optimization for a constant chord blade turbine yielded a C_p of 0.47 with flap-wise bending stresses of ∼210 MPa.
- For a constant chord blade design, a higher ΔP was observed across blade section near tip as compared to rest of the blade that leads to a non-uniform blade loading and is considered to be

detrimental to turbine life. This also implies a higher contribution of near tip part of the blade towards thrust and torque loading.

- Turbine blade geometries with variable chord and twist distribution along blade span resulted in entire blade surface contributing uniformly to thrust and torque loading thus improving hydro-structural performance of turbine.
- Hydro-structural optimization with a variable chord twisted blade turbine resulted in C_p of 0.55 (a 17% improvement compared to a constant chord design) with flap-wise bending stresses below 200 MPa.

ACKNOWLEDGMENTS

[1] D. G. Hall, K. S. Reeves, J. Brizzee, R. D. Lee, G. R. Carroll, and G. L. Sommers, "Wind and hydropower technologies, feasibility assessment of the water energy resources of the United States for new low power and small hydro classes of hydroelectric plants," Technical Report-Doe-Id-11263, U.S. Department of Energy, Energy Efficiency, and Renewable Energy, Idaho National Laboratory, 2006.

[2] A. Date and A. Akbarzadeh, "Design and cost analysis of low head simple reaction hydro turbine for remote area power supply," Renewable Energy **34**, 409–415 (2009).

[3] S. A. Korpela, *Principles of Turbomachinery*, 1st ed. (Wiley, Hoboken, New Jersey, 2011), p. 457.

[4] C. A. Consul, R. H. J. Willden, E. Ferrer, and M. D. McCulloch, "Influence of solidity on the performance of a cross-flow turbine," in Proceedings of the 8th European Wave And Tidal Energy Conference, 2009.

[5] U.S. Energy Information Administration "Annual energy review," in *Office of Energy Statistics* (U.S. Energy Information Administration: Washington, DC 20585, 2011).

[6] K. Bracmort, C. V. Stern, and V. Adam, *Hydropower: Federal and Nonfederal Investment* (Congressional Research Service, 2013).

[7] World Commission on Dams *Dams and Developement—A New Framework for Decision Making* (World Commission on Dams, 2000).

[8] D. G. Hall, S. J. Cherry, K. S. Reeves, R. D. Lee, G. R. Carroll, G. L. Sommers, and K. L. Verdin, *Water Energy Resources of the United States with Emphasis on Low Head/Low Power Resources*, edited by, I.N.E. and Environmental Laboratory (U.S. Department of Energy, 2004).

[9] M. S. Guney and K. Kaygusuz, "Hydrokinetic energy conversion systems: A technology status review," Renewable Sustainable Energy Rev. **14**, 2996–3004 (2010).

[10] P. Jacobson, *Assessment and Mapping of the Riverine Hydrokinetic Resource in the Continental United States* (Electric Power Research Institute, Palo Alto, CA, 2012).

[11] K. A. Haas, H. M. Fritz, S. P. French, B. T. Smith, and V. Neary, *The Assessment of Energy Production Potential from Tidal Streams in the United States* (Georgia Tech Research Corporation, 2011).

[12] M. M. Duquette and J. Swanson, "Solidity and blade number effects on a fixed pitch, 50w horizontal axis wind turbine," Wind Eng. **27**, 299–316 (2003).

[13] M. M. Duquette and K. D. Visser, "Numerical implications of solidity and blade number on rotor performance of horizontal axis wind turbines," J. Sol. Energy Eng. **125**, 425–432 (2003).

[14] L. Myers and A. S. Bahaj, "Wake studies of a 1/30th scale horizontal axis marine current turbine," Ocean Eng. **34**, 758–762 (2007).

[15] L. Myers and A. S. Bahaj, "Power output performance characteristics of a horizontal axis marine current turbine," Renewable Energy **31**, 197–208 (2006).

[16] L. E. Myers and A. S. Bahaj, "Experimental analysis of the flow field around horizontal axis tidal turbines by use of scale mesh disk rotor simulators," Ocean Eng. **37**, 218–227 (2010).

[17] V. S. Neary, A. A. Fontaine, P. Bachant, B. Gunawan, M. Wosnik, C. Michelen, and B. Straka, "US Department of Energy, National Lab Activities in Marine Hydrokinetics: Scaled model testing of doe reference turbines," in 10th European Wave and Tidal Energy Conference, Aalborg, Denmark, 2–5 September 2013.

[18] V. S. Neary, B. Gunawan, C. Hill, and L. P. Chamorro, "Near and far field flow disturbances induced by model hydrokinetic turbine: Adv and Adp comparison," Renewable Energy **60**, 1–6 (2013).

[19] H. Glauert, "Airplane Propellers," in *Aerodynamic Theory*, edited by W. F. Durand (Springer Verlag, Berlin, 1935).

[20] J. N. Sørensen, "Aerodynamic aspects of wind energy conversion," Annu. Rev. Fluid Mech. **43**, 427–448 (2011).

[21] J. L. Hess, "Panel methods in computational fluid dynamics," Annu. Rev. Fluid Mech. **22**, 255–274 (1990).

[22] Y. L. Young, M. R. Motley, and R. W. Yeung, "Three-dimensional numerical modeling of the transient fluid-structural interaction response of tidal turbines," J. Offshore Mech. Arct. Eng. **132**, 011101 (2010).

[23] J. C. Murray and M. Barone, "The development of cactus, a wind and marine turbine performance simulation code," AIAA Paper 2011-147, 2011.

[24] S. S. Mukherji, N. Kolekar, A. Banerjee, and R. Mishra, "Numerical investigation and evaluation of optimum hydrodynamic performance of a horizontal axis hydrokinetic turbine," J. Renewable Sustainable Energy **3**, 063105 (2011).

[25] S. Kang, I. Borazjani, J. A. Colby, and F. Sotiropoulos, "Numerical simulation of 3d flow past a real marine hydrokinetic turbine," Adv. Water Resour. **39**, 33–43 (2012).

[26]C. A. Consul, R. H. J. Willden, and S. C. McIntosh, "Blockage effects on the hydrodynamic performance of a marine cross-flow turbine," Philos. Trans. R. Soc. London, Ser. A **371**, 20120299 (2013).

[27]M. J. Churchfield, Y. Li, and P. J. Moriarty, "A large-eddy simulation study of wake propagation and power production in an array of tidal-current turbines," Philos. Trans. R. Soc. London, Ser. A **371**, 20120421 (2013).

[28]W. M. J. Batten, M. E. Harrison, and A. S. Bahaj, "Accuracy of the actuator disc-rans approach for predicting the performance and wake of tidal turbines," Philos. Trans. R. Soc. London, Ser. A **371**, 20120293 (2013).

[29]I. S. Hwang, Y. H. Lee, and S. J. Kim, "Optimization of cycloidal water turbine and the performance improvement by individual blade control," Appl. Energy **86**, 1532–1540 (2009).

[30]T. Stallard, R. Collings, T. Feng, and J. Whelan, "Interactions between tidal turbine wakes: Experimental study of a group of three-bladed rotors," Philos. Trans. R. Soc. London, Ser. A **371**, 20120159 (2013).

[31]E. H. Dowell and K. C. Hall, "Modeling of fluid structure interactions," Annu. Rev. Fluid Mech. **33**, 445–490 (2001).

[32]*Arbitrary Lagrangian-Eulerian and Fluid-Structure Interaction: Numerical Simulation*, edited by M. Souli and J. B. David (ISTE—John Wiley and Sons, Inc., Hoboken, New Jersey, 2010).

[33]G. Hou, J. Wang, and A. Layton, "Numerical methods for fluid-structure interaction—A review," Commun. Comput. Phys. **12**, 337–377 (2012).

[34]Y. L. Young, "Fluid–structure interaction analysis of flexible composite marine propellers," J. Fluids Struct. **24**, 799–818 (2008).

[35]X. D. He, Y. Hong, and R. G. Wang, "Hydroelastic optimisation of a composite marine propeller in a non-uniform wake," Ocean Eng. **39**, 14–23 (2012).

[36]M. S. Selig and V. L. Coverstone-Carroll, "Application of a genetic algorithm to wind turbine design," J. Energy Resour. Technol. **118**, 22–28 (1996).

[37]M. A. Belessis, D. G. Stamos, and S. G. Voutsinas, "Investigation of the capabilities of a genetic optimization algorithm in designing wind turbine rotors," in Proceedings of the European Union Wind Energy Conference and Exhibition, 1996.

[38]P. Fuglsang and H. A. Madsen, "Optimization method for wind turbine rotors," J. Wind. Eng. Ind. Aerodyn. **80**, 191–206 (1999).

[39]A. Betz, *Der Maximum Der Theoretisch Mölichen Ausnützung Des Windes Durch Windmotoren (the Maximum of the Theoretically Possible Exploitation of the Wind by Wind Motors)* (Zeitschrift für das Gesamte Turbinenwesen, 1920), Vol. 17.

[40]A. Betz, *Windenergie Und Ihre Ausnutzung Durch Windmühen (Wind Energy and Its Application by Windmills)* (Zeitschrift für das Gesamte Turbinenwesen, Göttingen, 1926).

[41]N. Kolekar, Z. Hu, A. Banerjee, and X. Du, "Hydrodynamic design and optimization of hydro-kinetic turbines using a robust design method," in Proceedings of the 1st Marine Energy Technology Symposium, METS13, Washington, D.C., 2013.

[42]J. F. Manwell, J. G. McGowan, and A. L. Rogers, *Wind Energy Explained: Theory, Design, and Application* (John Wiley and Sons, New York, 2009), Vol. 2.

[43]D. Mark and Y. Harold, *Xfoil, Subsonic Airfoil Development System.*, see http://web.mit.edu/drela/Public/web/xfoil/.

[44]D. Mark and Y. Harold, *Xfoil User Guide*.

[45]J. Degroote, K.-J. Bathe, and J. Vierendeels, "Performance of a new partitioned procedure versus a monolithic procedure in fluid-structure interaction," Comput. Struct. **87**, 793–801 (2009).

[46]N. Kolekar, S. S. Mukherji, and A. Banerjee, "Numerical modeling and optimization of hydrokinetic turbine," in *ASME 2011 5th International Conference on Energy Sustainability* (ASME, Washington DC, USA, 2011).

[47]*Ansys Cfx 14 User's Guide*, ANSYS, Inc., 2011.

[48]*Ansys Fluent 14.0 Theory Guide*, ANSYS, Inc., 2011.

[49]*Ansys Cfx 14 Theory Guide*, ANSYS, Inc., 2011.

[50]F. R. Menter, "Two-equation eddy-viscosity turbulence models for engineering applications," AIAA J. **32**, 1598–1605 (1994).

[51]F. R. Menter, "Performance of popular turbulence models for attached and separated adverse pressure gradient flows," AIAA J. **30**, 2066–2072 (1992).

[52]L. J. Vermeer, J. N. Sorensen, and A. Crespo, "Wind turbine wake aerodynamics," Prog. Aerosp. Sci. **39**, 467–510 (2003).

[53]D. C. Wilcox, *Turbulence Modeling for Cfd*, 3rd ed. (DCW Industries, La Canada, CA, 2006).

[54]P. Giguère and M. S. Selig, *Design of a Tapered and Twisted Blade for the Nrel Combined Experiment Rotor* (NREL: Golden, Colorado, 1999).

[55]H. A. Madsen, C. Bak, M. Døssing, R. Mikkelsen, and S. Øye, "Validation and modification of the blade element momentum theory based on comparisons with actuator disc simulations," Wind Energy **13**, 373–389 (2010).

[56]V. Neary, *Reference Inflow Characterization for River Resource Reference Model (Rm2)* (Oak Ridge National Laboratory, Oak Ridge, Tennessee, 2011).

[57]F. L. Ponta and H. Aref, "Numerical experiments on vortex shedding from an oscillating cylinder," J. Fluids Struct. **22**, 327–344 (2006).

[58]J. H. Holland, *Genetic Algorithms* (Scientific American, 1992).

[59]D. E. Goldberg, *Genetic Algorithms in Search, Optimization and Machine Learning* (Addison-Wesley Longman Publishing Co., Inc., 1989), p. 372.

[60]V. Okulov and J. N. Sørensen, "Maximum efficiency of wind turbine rotors using Joukowsky and Betz approaches," J. Fluid Mech. **649**, 497–508 (2010).

[61]P. Giguère and M. S. Selig, "New airfoils for small horizontal axis wind turbines," ASME J. Sol. Energy Eng. **120**, 108–114 (1998).

[62]Z. Hu, X. Du, N. Kolekar, and A. Banerjee, "Robust design with imprecise random variables and its application in hydro-kinetic turbine optimization," Eng. Optimiz. **2013**, 1–27.

[63]J. F. Manwell, J. G. McGowan, and A. L. Rogers, "Aerodynamics of wind turbines," in *Wind Energy Explained* (John Wiley & Sons, Ltd., 2009), pp. 91–155.